COMMUNICATION

Check for updates

Atomically precise Au_xAg_{25−x} nanoclusters with a modulated interstitial Au−Ag microenvironment for enhanced visible-light-driven photocatalytic hydrogen evolution†

Ye Liu,[a] Zhi Li,[b] Xiao-He Liu,[b] Nicola Pinna [ID] *[a] and Yu Wang [ID] *[a]

Herein, we report the study of atomically precise Au_xAg_{25−x} nanoclusters (NCs) toward photocatalytic hydrogen evolution. The incorporation of Au atoms into Ag_{25} NCs not only narrowed the HOMO−LUMO gaps but also created an interstitial Au−Ag microenvironment, which promoted the photogenerated charge carrier utilization and optimized the reaction dynamics.

Metal doping or alloying in heterogeneous catalysis provides opportunities to tailor the properties of catalysts, enhance their activity, selectivity and stability, and enable new catalytic reactions.[1–3] In the nanoparticle regime, bimetallic nanocrystals exhibit superior performance over individual metal nanocrystals due to the synergistic effect. By varying the ratio of the two metals, it is possible to control the surface composition and electronic structure of the nanocrystals, thus allowing for fine-tuning of the catalytic activity, selectivity, and reaction kinetics.[4–6] However, achieving precise atomic-level control over the composition of bimetallic nanocrystals is challenging due to synthetic limitations.

Metal nanoclusters (NCs), with atomic precision, represent a class of materials with tunable geometric structures at the atomic level.[7,8] This unique characteristic makes them ideal models for studying the relationship between defined NC structures and their physicochemical properties.[9–12] Furthermore, the broad light absorption within the UV-visible region and excellent stability in corrosive redox environments make metal NCs promising for solar energy conversion devices.[13–15] For instance, using a glutathione-protected Au_{18} NC as a sensitizer, a solar cell achieved a power conversion efficiency of 3.79%. Incorporating Ag into Au_{18} increased the efficiency to 4.22%.[16] Although the impact of hetero metal doping on the

New concepts

As one of the emerging light absorbing materials, metal nanoclusters with distinctive electronic structures have stimulated intensive research in solar energy conversion. In the past decade, efforts have been made towards the synthesis and structure determination of nanoclusters, while studies on the relationship between their structures and physiochemical properties are rare. Studying nanoclusters from the perspective of structure–activity relationships is of great significance to push nanoclusters into practical applications. In this work, we synthesized Au_{25}, Ag_{25} and alloy (AuAg)_{25} nanoclusters protected by 2,4-dimethylbenzenethiol, which were subsequently utilized as photosensitizers for photocatalytic hydrogen evolution. Physiochemical characterizations and DFT calculations allowed us to gain insight into the enhanced photocatalytic activities at the molecular level: a unique Au–Ag microenvironment was created by the simultaneous functioning of Au and Ag sites in the nanoclusters, which not only contributed to the separation of photogenerated charge carriers, but also balanced the hydrogen adsorption/desorption on the surface of the nanoclusters. Besides, alloying Au into Ag_{25} nanoclusters strengthened the light adsorption capabilities, which could also contribute to the photocatalytic activities. As a result, the reactivities of the alloy (AuAg)_{25} nanoclusters outperformed their single metal nanocluster counterparts (up to ∼5 times higher).

performance of pristine metal NCs has been extensively investigated, systematic studies on bimetallic NCs and their individual metal counterparts have been hindered by synthesis challenges.[17–23]

Due to the small size of metal NCs, they possess a high surface-to-volume ratio, with most of the metal atoms located on the surface and bound to ligands.[24,25] Since ligand affinities to different metals vary, the coordination modes and NC structures may differ.[10,26] As an example, the well-known Au_{25} NCs with a solved structure are protected by aliphatic 2-phenylethanethiol (PET), while the Ag_{25} NCs with a solved structure are protected with aromatic thiol. Doping Ag into Au_{25}(PET)_{18} successfully yields (AuAg)_{25}(PET)_{18}.[27] However, Ag_{25} NCs protected by PET remain unavailable.[28] Recently, Wang *et al.* reported a universal synthesis approach for preparing Au_{25} NCs protected by various aromatic thiols, enabling a comparison between the properties of bimetallic NCs and their
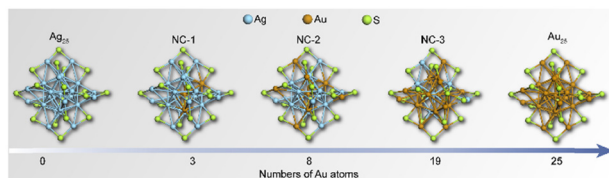
[a] *Department of Chemistry, IRIS Adlershof & The Center for the Science of Materials Berlin, Humboldt-Universität zu Berlin, 12489, Berlin, Germany.*
E-mail: nicola.pinna@hu-berlin.de, wangyuxx@hu-berlin.de

[b] *School of Geology and Environment, Xi'an University of Science and Technology, Xi'an 710049, Shaanxi, China*

† Electronic supplementary information (ESI) available. See DOI: https://doi.org/10.1039/d3nh00235g

Scheme 1   Schematic illustration of the Au_xAg_{25-x} NCs.

individual metal counterparts while maintaining the same ligand.[29]

In this study, Au_{25}, Ag_{25}, and $(AuAg)_{25}$ NCs protected by 2,4-dimethylbenzenethiol are synthesized and utilized as photosensitizers in a TiO_2-based system for photocatalytic H_2 production under visible light. To our surprise, the catalytic performance doesn't completely follow the order of the light absorption ability of the NCs. Although Au_{25} has the second narrowest highest occupied molecular orbital (HOMO)–lowest unoccupied molecular orbital (LUMO) gap among the five NCs, the hydrogen production rates of the bimetallic NC decorated TiO_2 systems outperform their single metal NC counterparts. DFT calculations reveal that the presence of Ag–Au dual metal sites could facilitate the formation of electron acceptor centers. In this way, the photoinduced electrons prefer to remain in the NCs for reducing the adsorbed hydrogen ions. Moreover, the Au–Ag environments in the bimetallic $(AuAg)_{25}$ NCs not only upshift the d-band centers (ε_d) but also balance the hydrogen adsorption/desorption dynamics, further optimizing the catalytic activities of the bimetallic NCs toward hydrogen production.

Scheme 1 shows the schematic illustration of the Au_xAg_{25-x} NCs. They were synthesized by the methods reported previously with some modifications (see ESI† for details).[28–31] The $(AuAg)_{25}$ NCs, namely NC-1, NC-2, and NC-3, consist of a series of bimetallic NCs, all sharing the common formula $[Au_xAg_{25-x}(SR)_{18}]^-$. Here, x varies within the following ranges: $1 \leq x \leq 3$ for NC-1, $3 \leq x \leq 8$ for NC-2, and $19 \leq x \leq 23$ for NC-3 (Fig. S1, ESI†). Tandem mass study revealed that there is a site preference for the metals (Fig. S2 and S3, ESI†). The UV-Vis absorption spectra in Fig. 1a showed different absorption profiles, where significant blue shifts were observed for NC-1, NC-2 and NC-3 when compared to the pristine Ag_{25} NCs. To gain a deeper insight into the absorption behaviors of the NCs, density functional theory calculations were performed. As is shown in Fig. 1b, the absorption bands located at around 675 nm and 488 nm correspond to the LUMO+1 ← HOMO−5 transition (α) and LUMO ← HOMO−4 (β) transition for Ag_{25} NCs, which are mainly contributed by the intraband transitions.
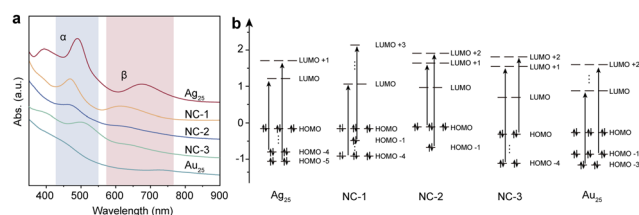
The Au_{25} NCs show similar transition behaviors compared to Ag_{25} NCs, while the excited electrons come from shallower HOMO states (LUMO ← HOMO−3 and LUMO+2 ← HOMO−1) for α and β transitions, respectively. However, the cases for the bimetallic NCs are different. The intraband transitions give rise to two absorption bands located at 612 nm and 468 nm, which could be assigned as LUMO+3 ← HOMO−1 transition (α) and LUMO ← HOMO−4 (β) transitions for NC-1 and LUMO+2 ← HOMO−1 transition (α) and LUMO+1 ← HOMO (β) for NC-2, respectively. As for NC-3, the α and β transitions arise from LUMO+1 ← HOMO−4 transitions and LUMO+2 ← HOMO transitions. Compared to Ag_{25} NCs, the HOMO–LUMO gaps decrease with the increase of the amount of Au atoms doped into the Ag_{25} NCs, with the values being 1.34 eV, 1.30 eV, 1.2 eV, 1.05 eV and 1.16 eV for Ag_{25}, NC-1, NC-2, NC-3 and Au_{25}, respectively (Table S1, ESI†).

The Kohn–Sham molecular orbitals (MO), energies, and atomic orbital (AO) contributions are shown in Fig. S4 (ESI†). Except for the main contribution from sp atomic orbitals of C and S atoms, the low-lying LUMO states and HOMO states of all the NCs were largely constructed from the d^{10} atomic orbitals of Ag and Au atoms, which constituted the d-bands. The LUMO state of Au_{25} was triply degenerated, while the others were doubly degenerated. It is also interesting to note that only the HOMO of NC-3 was doubly degenerated. It could also be concluded that the intraband α and β transitions originated from sp–sp transitions.

To investigate the photocatalytic activities of the NCs, we built a NCs/TiO_2 composite system to carry out the photocatalytic measurements. Accordingly, the composite samples were named NC-3/TiO_2, NC-2/TiO_2, NC-1/TiO_2, Au_{25}/TiO_2 and Ag_{25}/TiO_2. TiO_2 is known to be inactive in the visible region due to its large band gap, limiting its photoresponse.[32] To overcome this limitation, photosensitizers are often employed to extend the photoresponse of titania.[33,34] One effective approach to further improve the catalytic performance is narrowing the HOMO–LUMO gap of the light absorber, which enhances the light absorption of the composite. Fig. 2a and Fig. S5 (ESI†) demonstrate that TiO_2 decorated with metal NCs exhibits a favorable response to visible light. Among the four NC-based composites, Ag_{25}/TiO_2 displayed the lowest hydrogen evolution reaction (HER) rate at 2.45 μmol $g_{catal.}^{-1}$ h^{-1}, while NC-1/TiO_2 showed an HER rate of 6.65 μmol $g_{catal.}^{-1}$ h^{-1}. The HER rates of NC-2 and NC-3 significantly outweighed Ag_{25}/TiO_2 and Au_{25}/TiO_2, which reached 12.00 μmol $g_{catal.}^{-1}$ h^{-1} and 14.86 μmol $g_{catal.}^{-1}$ h^{-1}. This suggests that the doping of Au atoms into Ag_{25} significantly thus contributes to the catalytic activity of the system. It is worth noting that Au_{25} has a smaller HOMO–LUMO gap than NC-1 and NC-2. But surprisingly, the photocatalytic activities of either NC-1/TiO_2 or NC-2/TiO_2 outperform Au_{25}/TiO_2, indicating that the catalytic activities do not solely depend on the light absorption capabilities (Fig. 2a and Fig. S6, ESI†).

Previous studies have revealed the formation of a staggered energy level between small band gap metal NCs and n-type semiconductors upon band alignment.[35–37] The higher LUMO+X states compared to the conduction band (CB) of the semiconductor

Fig. 1   (a) UV-Vis absorption spectra of the as-prepared NCs; (b) transition states of the NCs.
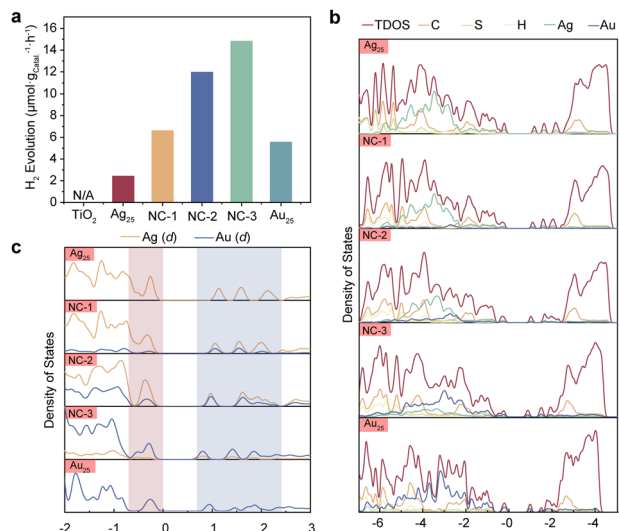
Fig. 2 (a) Hydrogen evolution under visible light irradiation. (b) Density of states projected to each atom. (c) Density of states projected to the d states of Ag and Au atoms.

Fig. 3 (a) The isosurfaces of charge density difference of H* adsorbed NCs; (b) the relationships of d-band center of the NCs; (c) the calculated free energy diagram of the HER on the motif scaffolds at the equilibrium potential, respectively.

facilitate the flow of photoinduced electrons from the LUMO+X states to the CB (Fig. S7, ESI†). However, there are other competitive pathways for these electrons. In the case of photo-excited dye systems, electrons on the LUMO can return to their ground state or participate in reduction reactions.[38] Since most dyes are catalytically inactive, hydrogen evolution only occurs when these electrons flow to the semiconductor. In contrast, metal NCs exhibit both photoactivity and catalytic activity.[39–41] Therefore, enhancing the composite's performance under visible light is achievable if the photoinduced electrons remain at the metal NCs and reduce the hydrogen ions adsorbed onto them. This proposed mechanism is illustrated in Fig. S8 (ESI†). In order to gain these molecular-level insights, we performed a series of DFT calculations, including the electronic structures and the charge dynamics when hydrogen was absorbed on the NC surface. Firstly, we started with the electronic structures of the NCs by comparing the projected density of states of the NCs. As it is shown in Fig. 2b, the HOMO and LUMO states were greatly contributed by the metallic d states from Ag and Au. Different from the case of pristine Ag_{25} NCs, the PDOS of Au atoms in the Au_{25} NCs exhibited broad distribution rather than isolated peaks within a wide range of energies of HOMO states (Fig. 2c). This indicates that the d states in the Au_{25} NCs are more delocalized than that in the pristine Ag_{25} NCs. Similar phenomena were also observed in the bimetallic clusters, indicating that alloying has a great impact on the electronic structures. It can also be observed that both the bonding and antibonding d states of Au have been strongly overlapped with the Ag counterparts in the bimetallic NCs. This overlapping PDOS of the d orbitals of the Ag and Au atoms suggests the formation of diffuse superatomic d-type orbitals, which could facilitate the transfer of hot electrons in space.[42,43]

Besides, the Bader charge and charge density difference analysis provided direct evidence for this electron transfer behavior. The net charges on each atom with a negative sign
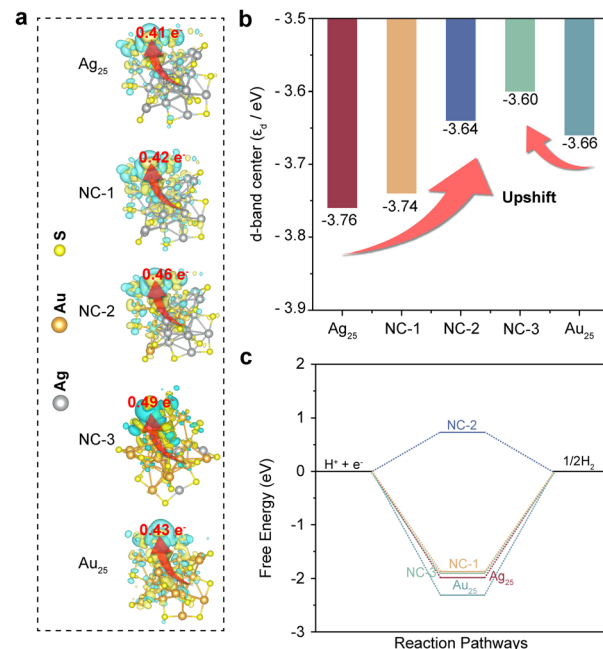
(depletion) indicating the loss of charge (positively charged) and a positive sign (accumulation) indicating the excess of charge (negatively charged). The calculated Bader charges of H* for hydrogen-adsorbing metal sites on each NC are shown in Fig. 3a, where the values were calculated to be 0.41 e⁻, 0.42 e⁻, 0.46 e⁻, 0.49 e⁻ and 0.43 e⁻ for Ag_{25}, NC-1, NC-2, NC-3 and Au_{25}, respectively. Therefore, electrons are more likely to be transferred to the adsorbed proton to catalyze the hydrogen evolution in bimetallic NCs, especially NC-3. Moreover, after the absorption of a hydrogen atom, all the bimetallic NCs displayed increased charge density area around both the Ag and Au site, which was clearly shown in the isosurfaces of charge density difference in Fig. 3a. Hence, the Au–Ag sites would be electron acceptor centers for catalyzing the hydrogen evolution, which is in accordance with the results obtained from Bader charge analysis.[24] Moreover, the d-band features (ε_d) of the clusters were also investigated. The ε_d of Au and Ag atoms in the bimetallic NCs showed upward shifts compared to the pristine Ag_{25} and Au_{25} NCs (Fig. 3b). The upward shift of ε_d would result in a decrease in the electron filling of the anti-bonding states, which could contribute to the adsorption of the reaction intermediate on the catalyst surface. In contrast, the downward shift of ε_d would facilitate the desorption of the reaction intermediate on the catalyst surface.[44–46] Based on the results obtained above, the impact of the dual metal sites on charge dynamics in the bimetallic NCs can be proposed. The introduction of Au sites into Ag_{25} NCs leads to the delocalization and hybridization of metallic d orbitals, forming diffuse supera-tomic d-type orbitals. As verified by Bader charge and charge density difference analysis, the diffuse superatomic d-type

orbitals can facilitate the transfer of photoinduced electrons to the adsorbed proton for photocatalytic reactions, which hinders the electrons from bulk recombination or migration to the CB of TiO_2. However, with the increase of the amount of Au sites in NC-3 the Ag_{25} NCs, the positive impact on the charge dynamics for HER reactions would decrease, as confirmed by the downward shifted ε_d and Bader charge values of Au_{25} compared to NC-2 and NC-3. Therefore, the unique microenvironment created by the Au–Ag dual metal sites also plays a vital role in optimizing the photocatalytic activities.

Moreover, further calculations from the perspective of reaction dynamics were performed to investigate the reaction pathways on the surfaces of the NCs. $H^+ + e^-$, adsorbed hydrogen (H*) and $1/2H_2$ were considered as the initial, intermediate and final states of the reaction, respectively. The calculated free energy diagrams of the HER process on the Ag atoms of each NC were presented in Fig. 3c. Ag_{25}, NC-1, NC-3 and Au_{25} NCs showed large upslopes with negative values of −1.95 eV, −1.94 eV, −1.86 eV and −2.31 eV, respectively, while NC-2 showed the smallest upslope with a positive value of 0.73 eV. However, the hydrogen adsorption/desorption was balanced by the Au–Ag sites because of orbital modulation, giving rise to the smallest upslope of 0.73 eV. Therefore, hydrogen desorption could be considered as the rate-determining step in the HER process for Ag_{25}, NC-1, NC-3 and Au_{25} NCs. Compared with Au_{25}, who had the largest upslope with a negative value of −2.31 eV, the other three clusters showed more positive free energy changes, especially in the case of NC-2. The interaction energy made them more energetically favored for hydrogen adsorption compared to Au_{25} NCs. It is reported that the reaction rate of the HER depends on the upslope process in the HER free energy diagram. With a much smaller positive upslope value, the interaction between hydrogen and the NC-2 surface would reach a more balanced hydrogen adsorption/desorption process involved in the HER process.[47–49] Combining the results obtained from ε_d and reaction free energy analysis, it is proved that the unique microenvironment created by the dual Au–Ag sites not only optimizes the charge dynamics, but also the adsorption/desorption of intermediates. As a result, the HER sites on the NCs were readily modulated, making the HER rates of the bimetallic NCs much faster than the pristine Ag_{25} and Au_{25} counterparts.

Conclusions

In summary, we have studied the sensitizing capabilities and reaction dynamics of bimetallic Au_xAg_{25-x} NCs toward visible-light-driven photocatalytic hydrogen evolution. The incorporation of Au atoms into Ag_{25} NCs narrowed the HOMO–LUMO gaps and modified the electronic configurations of the NCs. The unique microenvironment created by the dual Au–Ag sites in the bimetallic NCs helped to form electron-acceptor sites and upshifted the d-band centers, which hinders the electrons from bulk recombination and promotes the H_2 evolution process. On the other hand, the simultaneous role of the dual metal sites offered moderate hydrogen adsorption/desorption dynamics,

which further optimized the overall photocatalytic process. As a result, the photocatalytic activities of the NCs followed an order of NC-3 > NC-2 > NC-1 > Au_{25} > Ag_{25}. These results provide molecular insights into the origin of the photocatalytic activities of NC-based materials.

Author contributions

Y. W. and N. P.: conceptualization. Y. L. synthesized all the NCs, and performed all the physiochemical characterizations and DFT calculations. X. H. L. and Z. L. conducted the photocatalysis experiments. Data plotting and analysis were performed by Y. L. The manuscript was drafted by Y. L. and Y. W. and then revised by all the co-authors.

Conflicts of interest

There are no conflicts to declare.

Acknowledgements

Notes and references

1 J. Ran, T. Y. Ma, G. Gao, X.-W. Du and S. Z. Qiao, *Energy Environ. Sci.*, 2015, **8**, 3708–3717.

2 W. Wu, Q. Zhang, X. Wang, C. Han, X. Shao, Y. Wang, J. Liu, Z. Li, X. Lu and M. Wu, *ACS Catal.*, 2017, **7**, 7267–7273.

3 H. Fakhouri, E. Salmon, X. Wei, S. Joly, C. Moulin, I. Russier-Antoine, P.-F. Brevet, X. Kang, M. Zhu and R. Antoine, *J. Phys. Chem. C*, 2022, **126**, 21094–21100.

4 H. Nishiyama, T. Yamada, M. Nakabayashi, Y. Maehara, M. Yamaguchi, Y. Kuromiya, Y. Nagatsuma, H. Tokudome, S. Akiyama, T. Watanabe, R. Narushima, S. Okunaka, N. Shibata, T. Takata, T. Hisatomi and K. Domen, *Nature*, 2021, **598**, 304–307.

5 P. Babu and B. Naik, *Inorg. Chem.*, 2020, **59**, 10824–10834.

6 J. Zhao, J. Liu, Z. Li, K. Wang, R. Shi, P. Wang, Q. Wang, G. I. N. Waterhouse, X. Wen and T. Zhang, *Nat. Commun.*, 2023, **14**, 1909.

7 P. Chakraborty, A. Nag, A. Chakraborty and T. Pradeep, *Acc. Chem. Res.*, 2019, **52**, 2–11.

8 S. Hossain, D. Hirayama, A. Ikeda, M. Ishimi, S. Funaki, A. Samanta, T. Kawawaki and Y. Negishi, *Aggregate*, 2023, **4**, e255.

9 Z. Qin, J. Zhang, C. Wan, S. Liu, H. Abroshan, R. Jin and G. Li, *Nat. Commun.*, 2020, **11**, 6019.

10 R. Jin, C. Zeng, M. Zhou and Y. Chen, *Chem. Rev.*, 2016, **116**, 10346–10413.

11 H. Qian, D. E. Jiang, G. Li, C. Gayathri, A. Das, R. R. Gil and R. Jin, *J. Am. Chem. Soc.*, 2012, **134**, 16159–16162.

12 Y. Liu, X. Chai, X. Cai, M. Chen, R. Jin, W. Ding and Y. Zhu, *Angew. Chem., Int. Ed.*, 2018, **57**, 9775–9779.

13 M. A. Abbas, P. V. Kamat and J. H. Bang, *ACS Energy Lett.*, 2018, **3**, 840–854.

14 M. S. Bootharaju, C. W. Lee, G. Deng, H. Kim, K. Lee, S. Lee, H. Chang, S. Lee, Y.-E. Sung, J. S. Yoo, N. Zheng and T. Hyeon, *Adv. Mater.*, 2023, **35**, 2207765.

15 F.-X. Xiao, S.-F. Hung, J. Miao, H.-Y. Wang, H. Yang and B. Liu, *Small*, 2015, **11**, 554–567.

16 M. H. Naveen, R. Khan, M. A. Abbas, E. Cho, G. J. Lee, H. Kim, E. Sim and J. H. Bang, *Chem. Sci.*, 2020, **11**, 6248–6255.

17 O. J. H. Chai, Z. Liu, T. Chen and J. Xie, *Nanoscale*, 2019, **11**, 20437–20448.

18 Q.-L. Mo, B.-J. Liu and F.-X. Xiao, *J. Phys. Chem. C*, 2021, **125**, 22421–22428.

19 Z. Gan, N. Xia and Z. Wu, *Acc. Chem. Res.*, 2018, **51**, 2774–2783.

20 S. Wang, Q. Li, X. Kang and M. Zhu, *Acc. Chem. Res.*, 2018, **51**, 2784–2792.

21 A. Ghosh, O. F. Mohammed and O. M. Bakr, *Acc. Chem. Res.*, 2018, **51**, 3094–3103.

22 S. Hossain, Y. Niihori, L. V. Nair, B. Kumar, W. Kurashige and Y. Negishi, *Acc. Chem. Res.*, 2018, **51**, 3114–3124.

23 S. Sharma, K. K. Chakrahari, J.-Y. Saillard and C. W. Liu, *Acc. Chem. Res.*, 2018, **51**, 2475–2483.

24 G. Hu, Z. Wu and D.-E. Jiang, *J. Mater. Chem. A*, 2018, **6**, 7532–7537.

25 Y. Wang, X.-K. Wan, L. Ren, H. Su, G. Li, S. Malola, S. Lin, Z. Tang, H. Häkkinen, B. K. Teo, Q.-M. Wang and N. Zheng, *J. Am. Chem. Soc.*, 2016, **138**, 3278–3281.

26 Y. Du, H. Sheng, D. Astruc and M. Zhu, *Chem. Rev.*, 2020, **120**, 526–622.

27 D. R. Kauffman, D. Alfonso, C. Matranga, H. Qian and R. Jin, *J. Phys. Chem. C*, 2013, **117**, 7914–7923.

28 C. P. Joshi, M. S. Bootharaju, M. J. Alhilaly and O. M. Bakr, *J. Am. Chem. Soc.*, 2015, **137**, 11578–11581.

29 Z. Lei, J. J. Li, Z. A. Nan, Z. G. Jiang and Q. M. Wang, *Angew. Chem., Int. Ed.*, 2021, **60**, 14415–14419.

30 Y. Negishi, T. Iwai and M. Ide, *Chem. Commun.*, 2010, **46**, 4713–4715.

31 M. S. Bootharaju, C. P. Joshi, M. R. Parida, O. F. Mohammed and O. M. Bakr, *Angew. Chem., Int. Ed.*, 2016, **55**, 922–926.

32 A. Fujishima and K. Honda, *Nature*, 1972, **238**, 37–38.

33 M. Lv, D. Zheng, M. Ye, J. Xiao, W. Guo, Y. Lai, L. Sun, C. Lin and J. Zuo, *Energy Environ. Sci.*, 2013, **6**, 1615–1622.

34 C. Yu, G. Li, S. Kumar, H. Kawasaki and R. Jin, *J. Phys. Chem. Lett.*, 2013, **4**, 2847–2852.

35 Y. Liu, D. Long, A. Springer, R. Wang, N. Koch, M. Schwalbe, N. Pinna and Y. Wang, *Sol. RRL*, 2023, **7**, 2201057.

36 Y. Wang, X. H. Liu, Q. Wang, M. Quick, S. A. Kovalenko, Q. Y. Chen, N. Koch and N. Pinna, *Angew. Chem., Int. Ed.*, 2020, **59**, 7748–7754.

37 X. H. Liu, Y. He, Z. Li, A. Cheng, Z. Song, Z. Yu, S. Chai, C. Cheng and C. He, *J. Colloid Interface Sci.*, 2023, **651**, 368–375.

38 S. Maity, S. Kolay, S. Ghosh, S. Chakraborty, D. Bain and A. Patra, *J. Phys. Chem. Lett.*, 2022, **13**, 5581–5588.

39 Y. Wang, X.-H. Liu, R. Wang, B. Cula, Z.-N. Chen, Q. Chen, N. Koch and N. Pinna, *J. Am. Chem. Soc.*, 2021, **143**, 9595–9600.

40 Y. Liu, E. Wierzbicka, A. Springer, N. Pinna and Y. Wang, *J. Phys. Chem. C*, 2022, **126**, 1778–1784.

41 Y. Wang, X.-H. Liu, S. A. Kovalenko, Q.-Y. Chen and N. Pinna, *Chem. – Eur. J.*, 2019, **25**, 4814–4820.

42 X. Yu, Y. Sun, W. W. Xu, J. Fan, J. Gao, X. Jiang, Y. Su and J. Zhao, *Nanoscale Horiz.*, 2022, **7**, 1192–1200.

43 Y.-Y. Liu, Z. Wei, S. Meng, R. Wang, X. Jiang, R. Huang, S.-S. Li and L.-W. Wang, *Phys. Rev. B*, 2021, **104**, 115310.

44 Y. Sun, X. Li, T. Zhang, K. Xu, Y. Yang, G. Chen, C. Li and Y. Xie, *Angew. Chem., Int. Ed.*, 2021, **60**, 21575–21582.

45 W. Wang, W. Geng, L. Zhang, Z. Zhao, Z. Zhang, T. Ma, C. Cheng, X. Liu, Y. Zhang and S. Li, *Small*, 2023, **19**, e2206808.

46 J. K. Norskov, F. Abild-Pedersen, F. Studt and T. Bligaard, *Proc. Natl. Acad. Sci. U. S. A.*, 2011, **108**, 937–943.

47 X. Chen, Y. Gu, G. Tao, Y. Pei, G. Wang and N. Cui, *J. Mater. Chem. A*, 2015, **3**, 18898–18905.

48 J. K. Nørskov, T. Bligaard, A. Logadottir, J. R. Kitchin, J. G. Chen, S. Pandelov and U. Stimming, *J. Electrochem. Soc.*, 2005, **152**, J23.

49 F. Li, G. F. Han, H. J. Noh, J. P. Jeon, I. Ahmad, S. Chen, C. Yang, Y. Bu, Z. Fu, Y. Lu and J. B. Baek, *Nat. Commun.*, 2019, **10**, 4060.